

SCIENTIFIC REPORTS



OPEN

Mode-evolution-based polarization rotation and coupling between silicon and hybrid plasmonic waveguides

Sangsik Kim & Minghao Qi

Received: 20 August 2015
Accepted: 17 November 2015
Published: 18 December 2015

Hybrid plasmonic (HP) modes allow strong optical field confinement and simultaneously low propagation loss, offering a potentially compact and efficient platform for on-chip photonic applications. However, their implementation is hampered by the low coupling efficiency between dielectric guided modes and HP modes, caused by mode mismatch and polarization difference. In this work, we present a mode-evolution-based polarization rotation and coupling structure that adiabatically rotates the TE mode in a silicon waveguide and couples it to the HP mode in a strip silicon-dielectric-metal waveguide. Simulation shows that high coupling factors of 92%, 78%, 75%, and 73% are achievable using Ag, Au, Al, and Cu as the metal cap, respectively, at a conversion length of about 5 μm . For an extremely broad wavelength range of 1300–1800 nm, the coupling factor is >64% with a Ag metal cap, and the total back-reflection power, including all the mode reflections and backscattering, is below -40 dB, due to the adiabatic mode transition. Our device does not require high-resolution lithography and is tolerant to fabrication variations and imperfections. These attributes together make our device suitable for optical transport systems spanning all telecommunication bands.

Silicon (Si) photonics, which utilizes core and cladding materials that are compatible with complementary metal-oxide semiconductor (CMOS) technology for light guiding, modulation and detection, is promising for high-bandwidth communication and interconnection between computing nodes, due to the well-developed, low-cost CMOS manufacturing^{1–5}. Further scaling down Si photonic devices for on-chip interconnects or information processing is hampered by, among others, the diffraction limit. Plasmonics in metallic nanostructures can confine light at subwavelength scale with enhanced field intensity^{6–10}, thus in many cases breaking the diffraction limit and increasing the operating bandwidth^{11–14}. The required power for an electro-optical modulation can also be reduced with increased light-matter interaction and reduced parasitic capacitance¹⁵. However, the use of plasmonic nanostructures is generally limited by the high optical loss in metals^{16,17}.

Recently, hybrid plasmonic (HP) waveguide structures have been proposed to reduce the high propagation loss of plasmonic waveguides^{8,9}. A typical HP waveguide consists of a Si core and a metal cap, in between which is a gap filled with a low-index material such as SiO₂. When the gap is small, e.g. 50 nm, about 60% of the electromagnetic field can be confined within the low-index material, resulting in both a moderate propagation loss and a high field confinement in a low-index medium^{8,18}. Electro-optical modulators¹⁵, nano-lasers¹⁰, ring-resonators¹⁹, and nonlinear optical devices²⁰, based on, or related to HP waveguides have been demonstrated. Recently, various types of HP waveguide configurations based on nano-ridges²¹, metal ribbon buried slots²², and Si-on-nitride gap plasmon²³ have been proposed at mid-infrared (MIR) to take advantage of the reduced propagation loss in plasmonic devices at these longer wavelengths, thus making HP waveguides attractive for MIR applications such as chemical and biological sensing^{24–26}. To capitalize on these promising attributes of HP waveguides and integrate this platform into practical systems, meanwhile, requires a highly efficient and robust coupler between HP and Si waveguides to interface with Si photonics.

Previously, several schemes of couplers from Si waveguide to dielectric-loaded plasmonic waveguide²⁷, metal-insulator-silicon-metal waveguide²⁸, and HP waveguide²⁹ have been proposed or demonstrated. Among them, the HP waveguide coupler design shows a broadband performance with a maximum coupling efficiency

School of Electrical and Computer Engineering and Birck Nanotechnology Center, Purdue University, West Lafayette, IN 47907 USA. Correspondence and requests for materials should be addressed to M.Q. (email: mqj@purdue.edu)

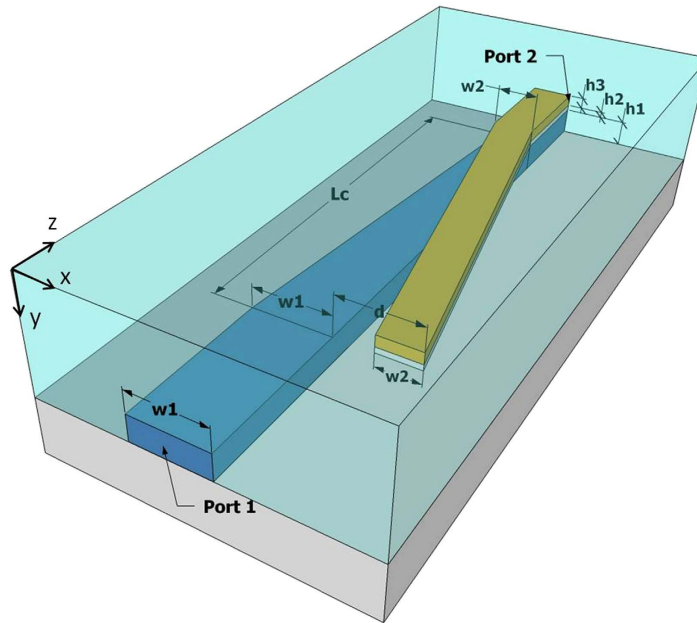


Figure 1. Schematic and geometric parameters of the mode-evolution-based polarization rotation and coupling structure. Metal cap and Si core are colored in yellow and blue, respectively, and SiO₂ substrate and cladding are colored in grey and cyan, respectively.

of about 70% at a gap size of 50 nm, from TM mode (electric field perpendicular to the surface) to HP mode²⁹. However, in Si photonic devices, TE mode (electric field parallel to the surface) is dominant due to its higher confinement and ease of fabrication. Thus, to fully utilize the HP waveguide in Si photonic devices, it is essential to have an efficient coupler between TE mode and HP mode, that is, to rotate the TE mode in a Si waveguide and simultaneously couple the rotated mode to the HP mode. Achieving simultaneously high coupling efficiency (>90% with metal propagation loss), low reflection (<30 dB as on-chip isolators are not readily available), broad bandwidth (preferably > 500 nm to cover all telecommunication bands), and high tolerance to fabrication imperfections is highly desirable for such devices to be incorporated into large-scale silicon photonics integration and manufacturing. Unfortunately, to the best of our knowledge, no such couplers have been reported.

In purely dielectric photonic systems, mode-evolution based polarization splitter and rotators have been demonstrated with high performance^{30–32}. Such devices usually include tapers to adiabatically splitting or rotating modes. However, simply tapering out the metal layer into sharp tips in a similar fashion does not achieve mode-evolution. Rather, the tapered sharp metal tip focuses and confines the light into the plasmonic mode^{33,34}.

Several polarization rotators consisting of plasmonic structures have been proposed^{13,35} or fabricated¹⁴ to reduce the device length for Si photonic applications. Such devices utilize asymmetric HP structures, covering the top and one side-wall of Si waveguide with oxide and metal³⁵ or tapering out the metal layer of HP waveguide^{13,14}. However, these designs did not focus on the coupling to hybrid modes and are based on mode-coupling³⁵ or a combination of mode-coupling and mode-evolution^{13,14}. For example, in Fig. 2 of ref. 13, the oscillation in polarization extinction ratio (PER) from 2 μm to 7 μm for the case of 90 nm spacer thickness is a signature of mode-coupling. Therefore it remains interesting to find a scheme to achieve pure mode-evolution when plasmonic effect is involved, and conduct a systematic investigation on the mechanism of transition between a dielectric mode and a HP mode.

In this paper, we present a truly mode-evolution-based polarization rotation and coupling (PRC) scheme that rotates the TE mode adiabatically and couples the rotated mode to the HP mode. When material absorption by metals is ignored, the coupler achieves almost 100% of efficiency with a proposed perfectly-phase-matched taper design. The performance of different metal caps (Cu, Au, Ag, and Al) with a linear Si taper is evaluated, and their spectral responses are assessed. Compared to mode-evolution structures in purely dielectric systems, our coupler has an upper limit of 92% efficiency when using silver as the metal cap, but it does have a much more compact size ($\sim 5 \mu\text{m}$) and broader bandwidths ($\sim 500 \text{ nm}$), which are desirable in future dense optical integration.

Device design

Figure 1 shows the schematic view of the mode-evolution-based PRC structure, and geometric parameters; w_1 and w_2 are the widths of Si waveguide at port 1 and HP waveguide at port 2, respectively, and h_1 , h_2 , and h_3 are the heights of Si core, SiO₂ spacer, and metal cap, respectively. The conversion/coupling region has a length of L_c , and starts when the lateral shift between the metal cap and Si core is d , and ends when the metal cap is exactly on top of the Si core. Through the conversion length L_c , the width of the Si core waveguide tapers from w_1 to w_2 , while that of the metal cap is fixed to w_2 .

We first calculate and plot the effective refractive indices of each mode in Fig. 2 as a function of Si core width (w_1 or w_2). Finite element method (FEM) is used for the calculation with a free space wavelength of $\lambda_0 = 1550 \text{ nm}$. The refractive indices of Si and SiO₂ are chosen to be $n_{\text{Si}} = 3.445$ and $n_{\text{SiO}_2} = 1.445$. For the metal cap we choose

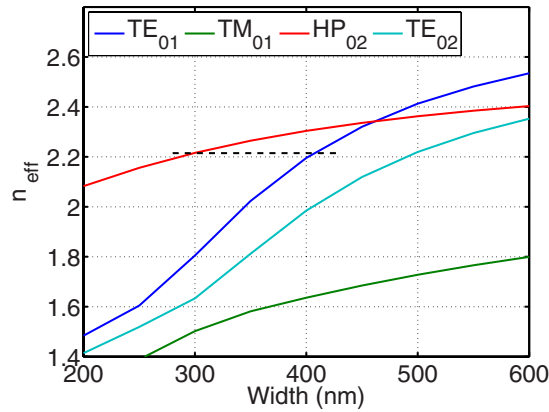


Figure 2. Effective refractive index of each mode, as a function of Si waveguide width, at i -th port (subscript); TE and TM modes at port 1 are plotted with blue and green lines respectively, and HP and TE modes at port 2 are plotted with red and cyan lines, respectively.

Cu for its CMOS compatibility, and the dispersive complex refractive index of Cu is used³⁶. Waveguide heights are fixed to $h_1 = 220$ nm, $h_2 = 30$ nm, and $h_3 = 100$ nm. Here, the thickness of SiO₂ spacer is chosen to strike a balance between the field confinement and propagation length for the subsequent hybrid mode^{8,9,18}. In general, a small spacer thickness is desirable as it would lead to strong field confinement in the spacer, which is one of the motivations to incorporate hybrid modes into the silicon photonics platform^{8,9,18}. A thinner spacer also requires an optimized coupler design as direct butt coupling would cause stronger reflection and scattering. Other thickness can also be selected to promote confinement over propagation loss or vice versa, and the coupler can be designed accordingly. The thickness of Si core is chosen to be compatible with common silicon-on-insulator (SOI) wafers. TE₀₁ (blue) and TM₀₁ (green) are the fundamental TE and TM modes at port 1, respectively, and HP₀₂ (red) and TE₀₂ (cyan) are the fundamental HP and TE modes at port 2, respectively. Our goal is to match the propagation constants (phases) between TE₀₁ and HP₀₂, while having a wide phase gap between TE₀₁ and TE₀₂. Here, we choose $w_2 = 300$ nm and $w_1 = 405$ nm as the port widths so that the phases of TE₀₁ and HP₀₂ modes are matched.

Figure 3(a) shows, from left to right, the normalized mode profiles ($|\mathbf{E}|$) at the cross-sections of the device with the separation distance $d = 600$ nm, 200 nm, and 0 nm, respectively, and the corresponding Si core width $w_1 = 405$ nm, 335 nm, and 300 nm. Note that the case of $d = 0$ nm is the same as the cross-section of port 2, and $d = 600$ nm is the cross-section at the beginning of the conversion region. TE₀₁ and SP₀₁ are the TE and surface plasmon modes at the interface between port 1 and PRC, respectively, and HP₀₂ and TE₀₂ are the HP and TE modes at port 2, respectively. PRC _{i} is the i -th PRC mode in a hybrid state. Upper figures (TE₀₁, PRC₀, and HP₀₂) are the main modes that play important roles in mode-evolution. This is an advantage over mode-coupling-based PRCs, where both PRC₀ and PRC₁ modes are excited for the rotation of polarization^{33,35}.

To see the phase variations of mode-evolution in more detail, the effective refractive indices of main (blue line) and secondary (dashed green line) modes are plotted in Fig. 3(b) as a function of separation distance d , and corresponding Si core width along the device. Notice that TE₀₁ mode is adiabatically evolved into HP₀₂ mode through PRC₀ mode (blue line), while simultaneously maintaining a large phase gap to their secondary modes (dashed green line).

Results and Discussion

The performance of mode-evolution-based PRC with linear Si taper is evaluated by calculating the coupling factor to the HP mode (CF_{HP}), which is defined as $CF_{\text{HP}} = P_{\text{HP}_{02}}/P_{\text{TE}_{01}}$, where $P_{\text{TE}_{01}}$ is the input power of TE₀₁ mode at port 1 and $P_{\text{HP}_{02}}$ is the output power of HP₀₂ mode at port 2. 3D FEM simulations are conducted by exciting TE₀₁ mode at port 1; then output fields of HP₀₂ mode is decomposed to calculate the $P_{\text{HP}_{02}}$ ^{33,37}.

Figure 4(a) shows the calculated CF_{HP} of the linearly tapered PRC as a function of L_c , with different metal caps: Cu (blue), Au (green), Ag (red), and Al (cyan). Simulation results with the output port width $w_2 = 300$ nm are plotted with plain lines, and those with different port widths $w_2 - 20$ nm and $w_2 + 20$ nm are also presented with dotted and dashed lines, respectively. To show the designed PRCs are truly based on mode-evolution, Cu metal cap without metallic absorption loss is also evaluated (circled blue line), and its CF_{HP} converges to about 97% after $L_c = 5$ μm . This is distinctively different from mode-coupling-based polarization rotation, which relies on the mode interference and the coupling factors show a sinusoidal oscillation as the conversion length increases^{13,14,33,35}. In reality when metal absorption cannot be ignored, CF_{HP} decreases monotonously as the L_c increases, after reaching a maximum point. The trend for CF_{HP} is similar with other metal caps, i.e., CF_{HP_0} hits the maximum point then decreases as L_c increases; however, each metal cap shows different maximum point and descent rate. Especially, with a Ag cap, the maximum CF_{HP} is $\sim 92\%$ and the descent rate is very slow, having over 80% of CF_{HP} throughout the conversion lengths of 4 μm to 15 μm . Furthermore, simulations for w_2 varied by ± 20 nm show almost identical results for each material, suggesting that the devices are tolerant to fabrication variations. This is another signature of the mode-evolution-based device and advantage over the mode-coupling-based one^{30,31}. Also, the conversion lengths for the maximum CF_{HP} are ultrashort with $L_c \sim 5$ μm . Typically, a mode-evolution-based device

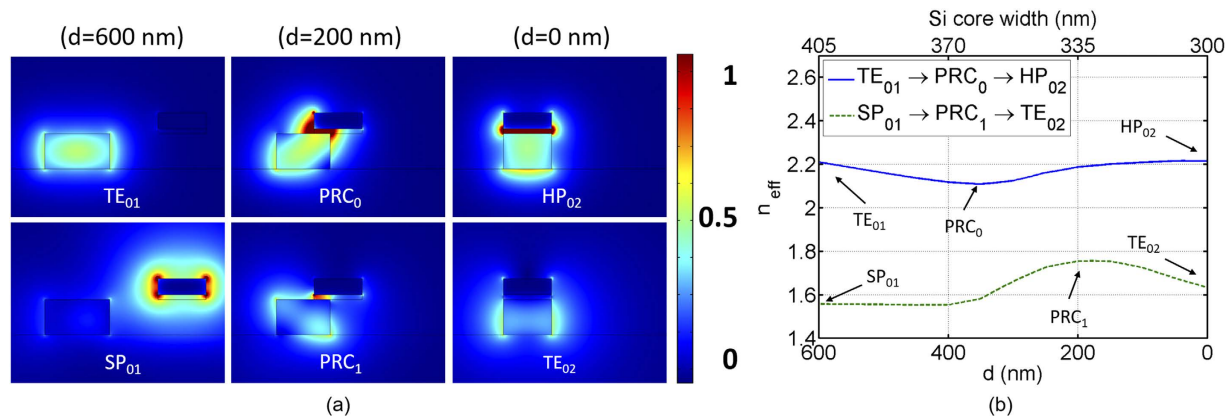


Figure 3. (a) Normalized mode profiles ($|E|$) at the cross-sections of the PRC structure when the separation distance is changed from $d = 600$ nm (port 1) to $d = 0$ nm (port 2). (b) Effective refractive indices as a function of separation distance d , and corresponding Si core width along the device. The main modes (TE_{01} , PRC_0 , and HP_{02}) and the secondary modes (SP_{01} , PRC_1 , and TE_{02}) are plotted in blue and dashed green, respectively.

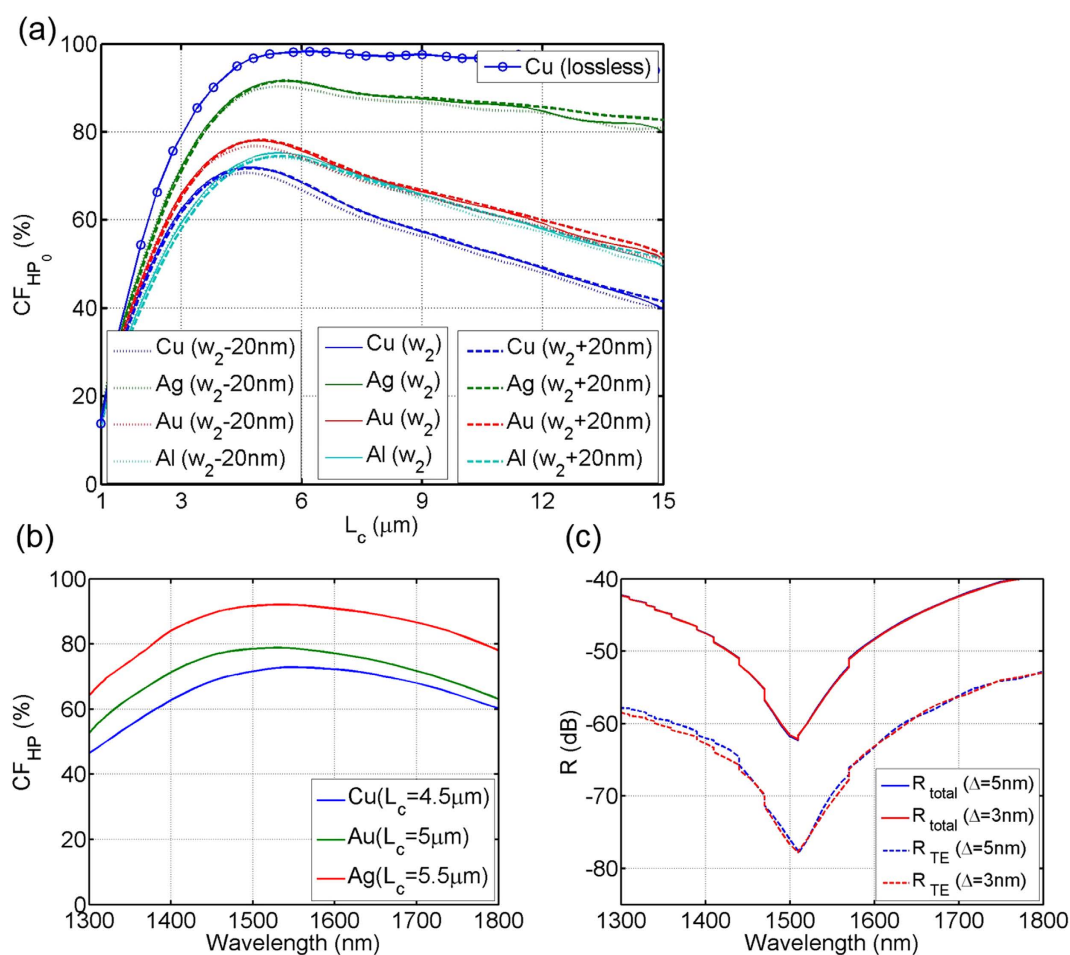


Figure 4. (a) Calculated CF_{HP_0} of the linearly tapered PRC as a function of L_c with different metal caps: Cu (blue), Au (green), Ag (red), and Al (cyan). Circled blue line is the case of Cu without metallic loss. Simulation results with different port widths of $w_2 + 20$ nm and $w_2 - 20$ nm are also presented with dashed and dotted lines, respectively. (b) CF_{HP_0} of the same devices as a function of λ_0 : Cu with $L_c = 4.5 \mu\text{m}$ (blue), Au with $L_c = 5.0 \mu\text{m}$ (green), and Ag with $L_c = 5.5 \mu\text{m}$ (red). (c) Calculated back-reflection power R spectrum of the linearly tapered PRC with different mesh grid size: $\Delta = 5$ nm (blue lines) and $\Delta = 3$ nm (red lines). Solid lines are the total back-reflection power (R_{total}) and dashed lines are the TE component of the total back-reflection (R_{TE}). Cu is used as the metal cap, and the $L_c = 4.5 \mu\text{m}$.

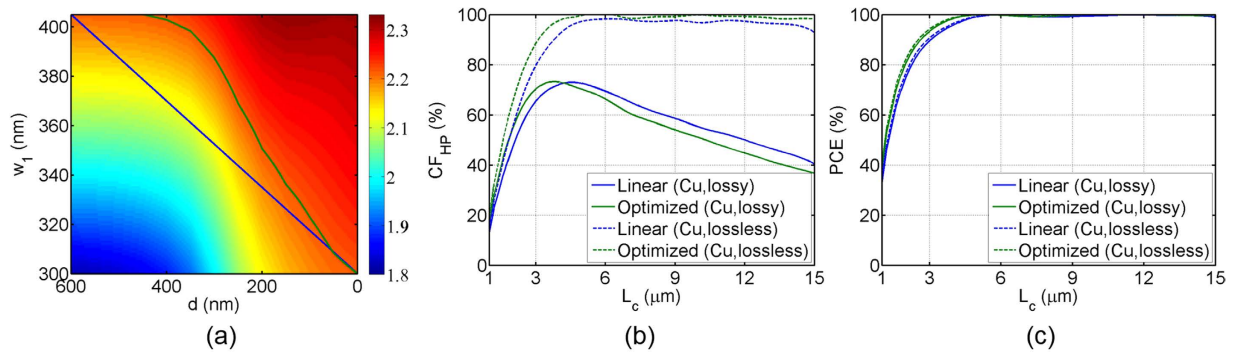


Figure 5. (a) Effective refractive index map of the fundamental modes (TE_{01} , PRC_0 , or HP_{02}), as functions of separation distance d and Si core width w_1 . Blue and green lines are the cases of linear and optimized (perfectly-phase-matched) taperings, respectively. Calculated (b) CF_{HP} and (c) PCE as a function of L_c for linear (blue) and optimized (green) taperings. Thick and dashed lines are the lossy and lossless cases, respectively.

requires a long device length, e.g., hundreds of micrometers, to smoothly convert the mode adiabatically^{30,31}; however, an ultrashort conversion length is achieved here, with a higher degree of field confinement in the HP mode

In addition to high coupling efficiency, couplers need to have broad bandwidth to cover a wide range of operating wavelengths. The spectral responses of the linearly tapered PRC are shown in Fig. 4(b), for Cu (blue), Au (green), and Ag (red) metal caps. For each metal cap, different conversion lengths are chosen, which correspond to their maximum CF_{HP} in Fig. 4(a): $4.5 \mu\text{m}$, $5.0 \mu\text{m}$, and $5.5 \mu\text{m}$ for Cu, Au, and Ag, respectively. Notice that, in every case, the spectral ranges with $CF_{HP} \geq 50\%$ are at least over 500 nm, covering the entire telecommunication bands.

In optical telecommunication systems, low back-reflection, or high return loss is also an important factor, especially for the emerging coherent transmission schemes. Despite recent advances^{38,39}, on-chip optical isolators are not readily available, so a close-to-zero reflection is highly important if a device is to be considered for practical use. Figure 4(c) shows the calculated back reflection power of the linearly tapered PRC as a function of free space wavelengths. Cu is used as the metal cap, and the device length is set to $L_c = 4.5 \mu\text{m}$. Solid lines are the total back-propagation power (R_{total}), accounting all possible reflections and scatterings. Dashed lines are the TE mode component of the total back-propagation (R_{TE}). Simulations with two different mesh grid sizes (Δ) were included: $\Delta = 5 \text{ nm}$ (blue lines) and $\Delta = 3 \text{ nm}$ (red lines), and the results are almost identical, suggesting high likelihood of truthfulness. Overall the total back-propagating power is below -40 dB for the entire telecommunication wavelength range of 1300–1800 nm. Note that previous HP mode couplers showed about 2–4% of back-reflections²⁹, but our mode-evolution based HP coupler shows an extremely low back-reflection, because our coupling mechanism is based on the mode-evolution, which allows an adiabatic and smooth mode transition.

Taper shape optimization. To further optimize the mode-evolution, the effective refractive indices of the main modes are calculated as functions of both w_1 and d , while the other geometric parameters are fixed; then the index map is plotted in Fig. 5(a), again with Cu as the metal cap. The blue line on the figure is the case of linear tapering as in Fig. 3(b), and the green curved line delineate the contour of the Si waveguide taper whose main mode (PRC_0) has the same effective refractive index as the HP_{02} mode. Note that the lower-right corner ($d = 0 \text{ nm}$ and $w_1 = 300 \text{ nm}$) is the point of pure HP_{02} mode, and the end-points on top ($w_1 = 405 \text{ nm}$) are the points of pure TE_{01} mode. Keeping the separation distance d linearly, the Si waveguide core width w_1 is tapered along the contour green line in Fig. 5(a); this tapering results in a perfect-phase-matching through the device. While there is a small phase deviation on PRC_0 mode with a linear tapering (as the blue line in Fig. 3(b)), such deviation is removed with the contoured taper, which gives a perfect-phase-matching throughout the device. Figure 5(b) shows the calculated CF_{HP} as a function of L_c for both tapers: blue lines for linear taper and green lines for perfectly-phase-matched (optimized) taper. Cases without considering the metal absorption are also plotted with dashed lines. Compared to linearly tapered design, perfectly-phase-matched tapering has shorter L_c for the maximum CF_{HP} point, and a little bit higher coupling factor for the case without metal absorption. The shorter L_c of perfectly-phase-matched tapering is due to the optimized separation distance d , making the effective interaction length longer. In terms of the coupling factor, even in the case without metal absorption, there is about 3% of loss with linear tapering (dashed blue line); this loss is due to the scattering that comes from the phase-mismatch, and is removed by an optimized taper which gives the perfect phase-matching (dashed green line). After including absorption losses (thick lines), however, there is no appreciable improvement in coupling factor. This indicates that, in this mode-evolution-based PRC, the phase-mismatch is not a significant factor that determines the maximum coupling factor. Rather, as we've seen in Fig. 4(a,b), the metallic losses are the dominant factor that determines the maximum CF_{HP} . The polarization conversion efficiency (PCE), which is defined as $PCE = P_{HP_{02}} / (P_{TE_{02}} + P_{HP_{02}})$, is also plotted in Fig. 5(c). Notice that the PCE s are almost 100% after $L_c = 5 \mu\text{m}$ for every case. This shows that there are no remaining TE mode for these mode-evolution based PRCs after a short conversion length of merely $L_c = 5 \mu\text{m}$.

Outline of device fabrication. In this section we describe briefly a potential route of fabrication for our proposed device. The fabrication can start from the deposition of a thin (e.g. 70 nm-thick) sacrificial silicon nitride (SiN) layer on top of the 220 nm-thick Si layer of a silicon-on-insulator (SOI) wafer. After the definition of Si waveguide via lithography and etching through the SiN and Si layers, a thick SiO₂ layer will be deposited to cover the Si waveguides. Chemical mechanical polishing (CMP) can be applied to planarize the SiO₂ top surface and the polishing will stop at the height of the top surface of the Si waveguide, using silicon nitride as the etch/polish stop. After removing the remaining SiN sacrificial layer, a 30 nm-thick layer of SiO₂ can be deposited on the planarized surface with high precision in thickness to form the spacer between the Si and metal layers. The metal layers can be subsequently formed with lithography and lift-off to complete the fabrication of our device. To make the structure more robust, we propose to over clad the metal structures with SiO₂ so that the metal is encapsulated between two SiO₂ layers. The fabrication process does not require high-resolution lithography as all lateral features are above 300 nm, which can be achieved with any deep-UV projection lithography tools currently available in most CMOS manufacturing facilities.

Conclusion

In summary, we present a mode-evolution-based polarization rotation and coupling scheme that has a high coupling efficiency (the maximum CF_{HP} is about 92% using Ag), an ultra-broad bandwidth (the spectral range with $CF_{HP} > 64\%$ is over 500 nm), and near-zero reflection. Also, the device length is very short ($L_c \sim 5 \mu\text{m}$) and is tolerant to fabrication errors. The material property of plasmonic metal cap is important to the device performances such as the maximum coupling factor and the bandwidth. The Si waveguide core widths are also optimized with a perfect-phase-matching, reducing the conversion length and removing the scattering loss. This mode-evolution-based PRC scheme could meet the stringent requirements in optical communications systems and should be useful in HP-waveguide-based applications such as electro-optical modulators¹⁵, nano-lasers¹⁰, ring-resonators¹⁹, nonlinear optical devices²⁰, and quantum plasmonic devices^{40–42}.

References

- Lipson, M. Guiding, modulating, and emitting light on silicon—challenges and opportunities. *J. Lightwave Technol.* **23**, 4222 (2005).
- Kirchain, R. & Kimerling, L. A roadmap for nanophotonics. *Nature Photon.* **1**, 303–305 (2007).
- Soref, R. The past, present, and future of silicon photonics. *IEEE J. Sel. Topics Quantum Electron.* **12**, 1678–1687 (2006).
- Jalali, B. & Fathpour, S. Silicon photonics. *J. Lightwave Technol.* **24**, 4600–4615 (2006).
- Vlasov, Y. A., O’Boyle, M., Hamann, H. F. & McNab, S. J. Active control of slow light on a chip with photonic crystal waveguides. *Nature* **438**, 65–69 (2005).
- Sorger, V. J., Oulton, R. F., Ma, R.-M. & Zhang, X. Toward integrated plasmonic circuits. *MRS bulletin* **37**, 728–738 (2012).
- Brongersma, M. L. & Shalaev, V. M. Applied physics the case for plasmonics. *Science* **328**, 440–441 (2010).
- Alam, M. Z., Aitchison, J. S. & Mojahedi, M. A marriage of convenience: Hybridization of surface plasmon and dielectric waveguide modes. *Laser Photon. Rev.* **8**, 394–408 (2014).
- Oulton, R. F., Sorger, V. J., Genov, D., Pile, D. & Zhang, X. A hybrid plasmonic waveguide for subwavelength confinement and long-range propagation. *Nature Photon.* **2**, 496–500 (2008).
- Oulton, R. F. *et al.* Plasmon lasers at deep subwavelength scale. *Nature* **461**, 629–632 (2009).
- Guan, X., Wu, H., Shi, Y., Wosinski, L. & Dai, D. Ultracompact and broadband polarization beam splitter utilizing the evanescent coupling between a hybrid plasmonic waveguide and a silicon nanowire. *Opt. Lett.* **38**, 3005–3008 (2013).
- Kim, S. & Qi, M. Copper nanorod array assisted silicon waveguide polarization beam splitter. *Opt. Express* **22**, 9508–9516 (2014).
- Caspers, J. N., Alam, M. & Mojahedi, M. Compact hybrid plasmonic polarization rotator. *Opt. Lett.* **37**, 4615–4617 (2012).
- Caspers, J. N., Aitchison, J. S. & Mojahedi, M. Experimental demonstration of an integrated hybrid plasmonic polarization rotator. *Opt. Lett.* **38**, 4054–4057 (2013).
- Sorger, V. J., Lanzillotti-Kimura, N. D., Ma, R.-M. & Zhang, X. Ultra-compact silicon nanophotonic modulator with broadband response. *Nanophotonics* **1**, 17–22 (2012).
- Boltasseva, A. & Atwater, H. A. Low-loss plasmonic metamaterials. *Science* **331**, 290–291 (2011).
- West, P. R. *et al.* Searching for better plasmonic materials. *Laser Photon. Rev.* **4**, 795–808 (2010).
- Dai, D. & He, S. Low-loss hybrid plasmonic waveguide with double low-index nano-slots. *Opt. Express* **18**, 17958–17966 (2010).
- Ketzaki, D. A., Tsilipakos, O., Yioultis, T. V. & Kriezis, E. E. Electromagnetically induced transparency with hybrid silicon-plasmonic traveling-wave resonators. *J. Appl. Phys.* **114**, 113107 (2013).
- Pitilakis, A. & Kriezis, E. E. Highly nonlinear hybrid silicon-plasmonic waveguides: analysis and optimization. *J. Opt. Soc. Am. B* **30**, 1954–1965 (2013).
- Mu, J. *et al.* Hybrid nano ridge plasmonic polaritons waveguides. *Appl. Phys. Lett.* **103**, 131107 (2013).
- Liang, H., Soref, R., Mu, J., Li, X. & Huang, W.-P. Long range mid-infrared propagation in si and ge hybrid plasmonic-photonic nano-ribbon waveguides. *Opt. Express* **22**, 28489–28499 (2014).
- Mu, J., Soref, R., Kimerling, L. C. & Michel, J. Silicon-on-nitride structures for mid-infrared gap-plasmon waveguiding. *Appl. Phys. Lett.* **104**, 031115 (2014).
- Soref, R. Mid-infrared photonics in silicon and germanium. *Nature Photon.* **4**, 495–497 (2010).
- Hu, J., Meyer, J., Richardson, K. & Shah, L. Feature issue introduction: mid-ir photonic materials. *Opt. Mater. Express* **3**, 1571–1575 (2013).
- Wang, J. *et al.* Monolithically integrated, resonant-cavity-enhanced dual-band mid-infrared photodetector on silicon. *Appl. Phys. Lett.* **100**, 211106 (2012).
- Briggs, R. M., Grandidier, J., Burgos, S. P., Feigenbaum, E. & Atwater, H. A. Efficient coupling between dielectric-loaded plasmonic and silicon photonic waveguides. *Nano Lett.* **10**, 4851–4857 (2010).
- Emboras, A. *et al.* Efficient coupler between silicon photonic and metal-insulator-silicon-metal plasmonic waveguides. *Appl. Phys. Lett.* **101**, 251117–251117 (2012).
- Song, Y., Wang, J., Li, Q., Yan, M. & Qiu, M. Broadband coupler between silicon waveguide and hybrid plasmonic waveguide. *Opt. Express* **18**, 13173–13179 (2010).
- Watts, M. & Haus, H. Integrated mode-evolution-based polarization rotators. *Opt. Lett.* **30**, 138–140 (2005).
- Watts, M., Haus, H. & Ippen, E. Integrated mode-evolution-based polarization splitter. *Opt. Lett.* **30**, 967–969 (2005).
- Watts, M. R. *et al.* Towards integrated polarization diversity: design, fabrication and characterization of integrated polarization splitters and rotators. In *Optical Fiber Communication Conference, PDP11* (Optical Society of America, 2005).
- Kim, S. & Qi, M. Polarization rotation and coupling between silicon waveguide and hybrid plasmonic waveguide. *Opt. Express* **23**, 9968–9978 (2015).

34. Luo, Y. *et al.* On-chip hybrid photonic-plasmonic light concentrator for nanofocusing in an integrated silicon photonics platform. *Nano Lett.* **15**, 849–856 (2015).
35. Jin, L., Chen, Q. & Wen, L. Mode-coupling polarization rotator based on plasmonic waveguide. *Opt. Lett.* **39**, 2798–2801 (2014).
36. Johnson, P. B. & Christy, R.-W. Optical constants of the noble metals. *Phys. Rev. B* **6**, 4370 (1972).
37. Yariv, A. & Yeh, P. *Photonics: Optical Electronics in Modern Communications* (Oxford University Press, Inc., 2006).
38. Fan, L. *et al.* An all-silicon passive optical diode. *Science* **335**, 447–450 (2012).
39. Bi, L. *et al.* On-chip optical isolation in monolithically integrated non-reciprocal optical resonators. *Nature Photon.* **5**, 758–762 (2011).
40. de Leon, N. P., Lukin, M. D. & Park, H. Quantum plasmonic circuits. *IEEE J. Sel. Topics Quantum Electron.* **18**, 1781–1791 (2012).
41. Tame, M. *et al.* Quantum plasmonics. *Nature Phys.* **9**, 329–340 (2013).
42. Fakonas, J. S., Lee, H., Kelaita, Y. A. & Atwater, H. A. Two-plasmon quantum interference. *Nature Photon.* **8**, 317–320 (2014).

Acknowledgements

This work is supported in part by National Science Foundation grant CMMI-1120577, Defense Threat Reduction Agency grants HDTRA110-1-0106 and HDTRA1-07-C-0042, National Institute of Health grant 1R01RR026273-01, Air Force Office of Scientific Research grant FA9550-12-1-0236, and DARPA PULSE program grant W31P40-13-1-0018 from AMRDEC.

Author Contributions

S.K. and M.Q. conceived the device design and wrote the manuscript. S.K. performed the numerical simulations.

Additional Information

Competing financial interests: The authors declare no competing financial interests.

How to cite this article: Kim, S. and Qi, M. Mode-evolution-based polarization rotation and coupling between silicon and hybrid plasmonic waveguides. *Sci. Rep.* **5**, 18378; doi: 10.1038/srep18378 (2015).



This work is licensed under a Creative Commons Attribution 4.0 International License. The images or other third party material in this article are included in the article's Creative Commons license, unless indicated otherwise in the credit line; if the material is not included under the Creative Commons license, users will need to obtain permission from the license holder to reproduce the material. To view a copy of this license, visit <http://creativecommons.org/licenses/by/4.0/>